

Deep Atrous Guided Filter for Image Restoration in Under Display Cameras

Varun Sundar*, Sumanth Hegde*, Divya Kothandaraman, and Kaushik Mitra

Indian Institute of Technology Madras

{varunsundar@smail, sumanth@smail, ee15b085@smail, kmitra@ee}.iitm.ac.in

Abstract. Under Display Cameras present a promising opportunity for phone manufacturers to achieve bezel-free displays by positioning the camera behind semi-transparent OLED screens. Unfortunately, such imaging systems suffer from severe image degradation due to light attenuation and diffraction effects. In this work, we present Deep Atrous Guided Filter (DAGF), a two-stage, end-to-end approach for image restoration in UDC systems. A Low-Resolution Network first restores image quality at low-resolution, which is subsequently used by the Guided Filter Network as a filtering input to produce a high-resolution output. Besides the initial downsampling, our low-resolution network uses multiple, parallel atrous convolutions to preserve spatial resolution and emulates multi-scale processing. Our approach’s ability to directly train on megapixel images results in significant performance improvement. We additionally propose a simple simulation scheme to pre-train our model and boost performance. Our overall framework ranks 2nd and 5th in the RLQ-TOD’20 UDC Challenge for POLED and TOLED displays, respectively.

Keywords: Under-Display Camera, Image Restoration, Image Enhancement.

1 Introduction

Under Display Cameras (UDC) promise greater flexibility to phone manufacturers by altering the traditional location of a smartphone’s front camera. Such systems place the camera lens behind the display screen, making truly bezel-free screens possible and maximising screen-to-body ratio. Mounting the camera at the centre of the display also offers other advantages such as enhanced video call experience and is more relevant for larger displays found in laptops and TVs. However, image quality is greatly degraded in such a setup, despite the superior light efficiency of recent display technology such as OLED screens [57]. As illustrated in Figure 1, UDC imaging systems suffer from a range of artefacts including colour degradation, noise amplification and low-light settings. This creates a need for restoration algorithms which can recover photorealistic scenes from UDC measurements.

* Equal Contribution

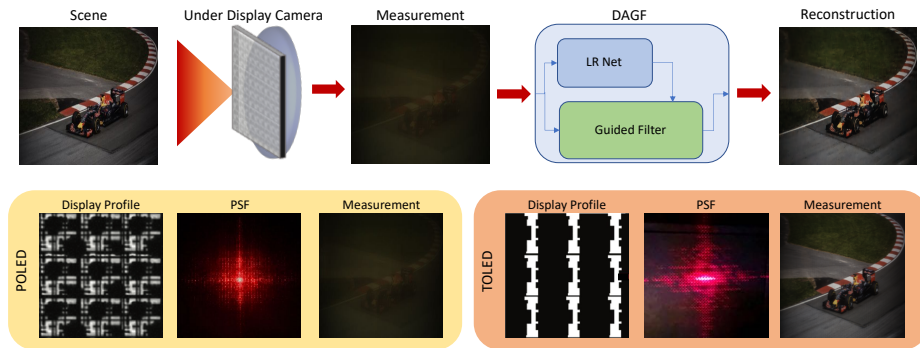


Fig. 1: Under Display Cameras [75] mount lenses behind semi-transparent OLED displays leading to image degradation. In this work, we introduce DAGF, which performs image restoration at megapixel resolution for both POLED and TOLED displays.

Learning based methods, accentuated by deep learning, have achieved state-of-the-art performance on a variety of image restoration tasks including deblurring [5,41,47], dehazing [3,6,44], denoising [1,66,68], deraining [6,30] and image enhancement [8,13]. However, deep learning techniques face two main drawbacks with regard to UDC imaging systems. First, such methods do not scale computationally with input image resolution, and are typically run on much smaller patches. This is problematic for restoring severely degraded images such as UDC measurements, since small patches lack sufficient context. Second, common Convolutional Neural Networks (CNNs) employed in image restoration use multiple down-sampling operations to stack more layers and expand their receptive field without blowing up their memory footprint. Down-sampling leads to a loss of spatial information and affects performance in pixel-level dense prediction tasks such as image restoration [5,10,38]. An alternative is to simply omit such sub-sampling and resort to atrous (or dilated) convolutions. Owing to memory constraints, this is not feasible since we deal with high-resolution images in UDC systems.

To overcome these drawbacks, we propose a two-stage, end-to-end trainable approach utilizing atrous convolutions in conjunction with guided filtering. The first stage performs image restoration at low-resolution using multiple, parallel atrous convolutions. This allows us to maximally preserve spatial information without an exorbitant memory requirement. The guided filter then uses the low-resolution output as the filtering input to produce a high-resolution output via joint upsampling. Our approach makes it possible to directly train on high resolution images, and results in significant performance gains. Our contributions are as follows:

- We propose a novel image restoration approach for UDC systems utilizing atrous convolutions in conjunction with guided filters (Section 3).

- We show that directly training on megapixel inputs allows our approach to significantly outperform existing methods (Section 4.3).
- We propose a simple simulation scheme to pre-train our model and further boost performance (Section 4.2).

Our code and simulated data is publicly available at [varun19299.github.io/deep-atrous-guided-filter/](https://github.com/varun19299/deep-atrous-guided-filter/).

2 Related Work

Image restoration encompasses tasks like image denoising, dehazing, deblurring and super resolution [1,3,36,41]. In recent years, deep learning has been the go-to tool in the field, with fully convolutional networks at the forefront of this success [37,45,50,65]. Of these, residual dense connections [71] exploiting hierarchical features has garnered interest with subsequent works in specific restoration tasks [6,25,44,64,71]. Another class of techniques use a GAN [15] based setting. Methods like [23,28] fall in this category. Finally, there exist recent work exploiting CNNs as an effective image prior [29,53,67]. However, the above-mentioned methods operate on small patches of the input image and do not scale to larger input dimensions.

Joint upsampling seeks to generate a high-resolution output, given a low-resolution input and a high-resolution guidance map. Joint Bilateral Upsampling [27] uses a bilateral filter towards this goal, obtaining a piecewise-smooth high-resolution output, but at a large computational cost. Bilateral Grid Upsampling [7] greatly alleviates this cost by fitting a grid of local affine models on low-resolution input-output pairs, which is then re-used at high resolution. Deep Bilateral Learning [13] integrates bilateral filters in an end-to-end framework, with local affine grids that can be learnt for a particular task.

Guided filters [19] serve as an alternative to Joint Bilateral Upsampling, with superior edge-preserving properties at a lower computational cost. Deep Guided Filtering [59] integrates this with fully convolutional networks and demonstrates it for common image processing tasks, with recent interest in the hyperspectral [17], remote [60] and medical imaging [14]. Guided filters have been mainly explored in the context of accelerating image processing operators. In our work, we present a different application of image restoration.

Atrous or dilated convolutions incorporate a larger receptive field without an increase in the number of parameters or losing spatial resolution. Yu *et al.* [62] proposed a residual network using dilated convolutions. Dilated convolutions have found success in semantic segmentation [8,73], dehazing [6,44] and deblurring [5] tasks as well as general image processing operations [11]. However, a major challenge in atrous networks is keeping memory consumption in check. Multi-scale fusion via pyramid pooling or encoder-decoder networks [9,10,32,40,67] can offload intensive computation to lower scales, but can lead to missing fine details. Instead, we include channel and pixel attention [44] to have a flexible receptive field at each stage while better tending to severely degraded regions.

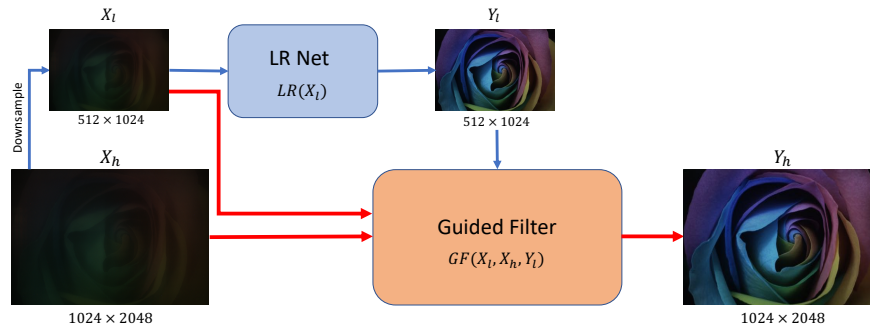


Fig 2: **Framework overview of DAGF.** Our architecture seeks to operate directly on megapixel images by performing joint upsampling. A low resolution network (LRNet) restores a downsampled version X_l of input X_h to produce Y_l . The guided filter then uses this to yield the final high-resolution output Y_h .

Compared to prior work, **our main novelty** lies in directly training on megapixel images by incorporating multiple, parallel smoothed atrous convolutions in a guided filter framework. This adapts the proposed framework in Wu *et al.* [59]- primarily developed for image processing tasks- to handle the challenging scenario of image restoration for Under Display Cameras.

3 Deep Atrous Guided Filter

To address the challenges posed by Under Display Cameras, we employ a learning based approach that directly trains on megapixel images. We argue that since UDC measurements are severely degraded, it is imperative to train models with large receptive fields on high-resolution images [26,47,48].

Our approach, **Deep Atrous Guided Filter Network (DAGF)**, consists of two stages: (a) Low Resolution Network (LRNet), which performs image restoration at a lower resolution, and (b) Guided Filter Network, which uses the restored low-resolution output and the high-resolution input to produce a high-resolution output. Our guided filter network, trained end-to-end with LRNet, restores content using the low-resolution output while preserving finer detail from the original input.

We design our approach to perform image restoration for two types of OLED displays: Pentile OLED (POLED) and Transparent OLED (TOLED). As seen in Figure 1, TOLED has a stripe pixel layout, while POLED has a pentile pixel layout with a much lower light transmittance. Consequently, TOLED results in a blurry image, while POLED results in a low-light, colour-distorted image.

3.1 LR Network

LRNet comprises of three key components: i) PixelShuffle [46] ii) atrous residual blocks, and iii) a gated attention mechanism [6,49]. We first use PixelShuffle

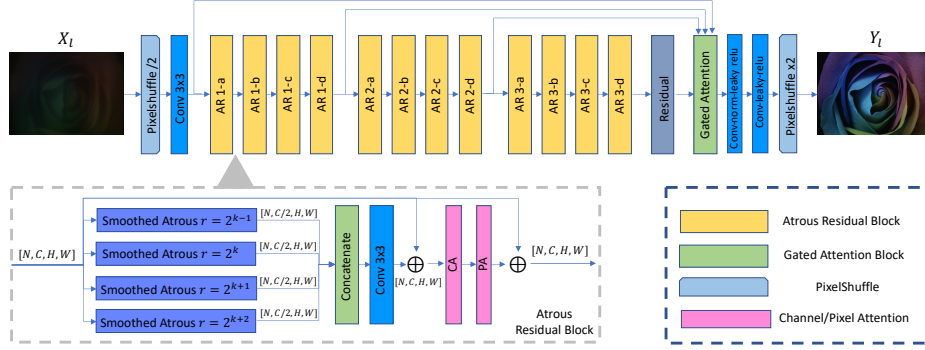


Fig. 3: **Overview of LRNet.** LRNet operates on a low-resolution version X_l of original input X_h . The input image X_l is downsampled via pixelshuffle, encoded via many atrous residual blocks and finally a gated attention mechanism aggregates contextual information to produce low-resolution output Y_l .

[46] to lower input spatial dimensions while expanding channel dimensions. This affords us a greater receptive field at a marginal memory footprint [16,31]. We further encode the input into feature maps via successive atrous residual blocks and then aggregate contextual information at multiple levels by using a gated attention mechanism. We now describe each component of LRNet.

Smoothed Atrous Convolutions. Unlike common fully convolutional networks employed in image restoration [16,31,39], which use multiple downsampling blocks, we opt to use atrous (or dilated) convolutions [61] instead. This allows us expand the network’s receptive field without loss in spatial resolution, which is beneficial for preserving fine detail in dense prediction tasks.

Atrous convolutions, however, lead to gridding artefacts in their outputs [18,54,56]. To alleviate this, we insert a convolution layer before each dilated convolution, implemented via shared separable kernels for computational and parameter efficiency [56]. Concretely, for an input feature map F^{in} with C channels, the smoothed atrous convolution layer produces output feature map F^{out} with C channels as follows:

$$F_i^{\text{out}} = \sum_{j \in [C]} ((F_j^{\text{in}} * K^{\text{sep}} + b_i) *_r K_{ij}) \quad (1)$$

where F_i^{out} is the i^{th} output channel, b_i is a scalar bias, $*$ is a 2D convolution and $*_r$ is a dilated convolution with dilation r . K_{ij} is a 3×3 convolution kernel and K^{sep} is the shared separable convolution kernel, shared among all input feature channels. For dilation rate r , we use a shared separable kernel of size $2r - 1$.

We also add adaptive normalization [11] and leaky rectified linear unit (LReLU) after the smoothed atrous convolution. LReLU may be represented as: $\Phi(x) =$

$\max(\alpha x, x)$, where we set $\alpha = 0.2$. Adaptive Normalization combines any normalization layer and the identity mapping as follows:

$$AN(F^{\text{in}}) = \lambda F^{\text{in}} + \mu N(F^{\text{in}}) \quad (2)$$

where F^{in} is the input feature map, $\lambda, \mu \in \mathbb{R}$ and $N(\cdot)$ is any normalization layer such as batch-norm [22] or instance-norm [52]. We use instance-norm in our adaptive normalization layers. In our ablative studies (Section 5.2), we show that our adaptive normalization layer results in improved performance.

Atrous Residual blocks. As depicted in Fig. 3, we propose to use multiple, parallel, smoothed atrous convolutions with various dilation rates in our residual blocks, following its recent success in image deblurring [5]. For atrous residual block AR- k , belonging to the k th group, we use four smoothed atrous convolutions with dilation rates $\{2^{k-1}, 2^k, 2^{k+1}, 2^{k+2}\}$. Each convolution outputs a feature map with $C/2$ channels, which we concatenate to obtain $2C$ channels. These are subsequently reduced to C channels via a 1×1 convolution. Our atrous residual blocks also utilize channel and pixel attention mechanisms, which are described below.

Channel Attention. We use the channel attention block proposed by Qin *et al.* [44]. Specifically for a feature map F^{in} of dimensions $C \times H \times W$, we obtain channel-wise weights by performing global average pooling (GAP) and further encode it via two 1×1 conv layers. We multiply F^{in} with these channel weights CA to yield output F^{out} :

$$GAP_i = \frac{1}{HW} \sum_{u \in [H], v \in [W]} F_i^{\text{in}}(u, v) \quad (3)$$

$$CA_i = \sigma \left(\sum_{j \in [C]} \Phi \left(\sum_{k \in [C/8]} GAP_k * K_{jk} + b_j \right) * K'_{ij} + b_i \right) \quad (4)$$

$$F_i^{\text{out}} = CA_i \odot F_i^{\text{in}} \quad (5)$$

where, σ is the sigmoid activation, Φ is LReLU described earlier and \odot is element-wise multiplication.

Pixel Attention. To account for uneven context distribution across pixels, we use a pixel attention module [44] that multiplies the input feature map F^{in} of shape $C \times H \times W$ with an attention map of shape $1 \times H \times W$ varying across pixels, but constant across channels. We obtain the pixel attention map PA by using two 1×1 conv layers:

$$PA = \sigma \left(\sum_{j \in [C/8]} \Phi \left(\sum_{k \in [C]} F_k^{\text{in}} * K_{jk} + b_j \right) * K'_j + b \right) \quad (6)$$

$$F_i^{\text{out}} = PA \odot F_i^{\text{in}} \quad (7)$$

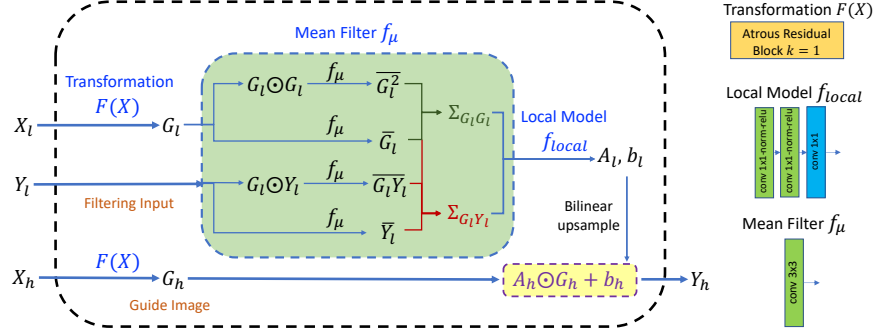


Fig. 4: **Computational Graph of Guided Filter Stage.** The guided filter first transforms the high-resolution input X_h to guide image G_h , and then yields the final output Y_h via joint upsampling. Our guided filter network is differentiable and end-to-end trainable [59].

Gated Attention. We utilise a gated attention mechanism [6,49] to aggregate information across several atrous residual blocks. Fusing features from different levels is beneficial for both low-level and high-level tasks [33,63,73]. We extract feature maps before the first atrous residual block (F^0), and right after each atrous residual group (F^1, \dots, F^k). For k atrous groups, we concatenate these $k + 1$ feature maps and output $k + 1$ masks, using \mathcal{G} , a 3×3 conv layer:

$$(\mathcal{M}^0, \mathcal{M}^1, \dots, \mathcal{M}^k) = \mathcal{G}(F^0, F^1, \dots, F^k) \quad (8)$$

$$F^{\text{out}} = \mathcal{M}^0 \odot F^0 + \sum_{l \in [k]} \mathcal{M}^l \odot F^l \quad (9)$$

3.2 Guided Filter Network

Given a high-resolution input X_h , low-resolution input X_l and low-resolution output Y_l , we seek to produce a high-resolution output Y_h , which is perceptually similar to Y_l while preserving fine detail from X_h . We adopt the guided filter proposed by He *et al.* [19,20] and use it in an end-to-end trainable fashion [59]. As illustrated in Figure 4, the guided filter formulates Y_h as:

$$Y_h = A_h \odot G_h + b_h \quad (10)$$

where $G_h = F(X_h)$ is a transformed version of input X_h . We bilinearly upsample A_h and b_h from low-resolution counterparts A_l and b_l , such that:

$$\bar{Y}_l = A_l \odot \bar{G}_l + b_l \quad (11)$$

where \bar{G}_l, \bar{Y}_l are mean filtered versions of G_l, Y_l , ie., $\bar{G}_l = f_\mu(G_l)$ and $\bar{Y}_l = f_\mu(Y_l)$. Compared to Wu *et al.* [59], we implement f_μ by a 3×3 convolution

(instead of a box-filter). Instead of directly inverting Equation 11, we obtain its solution using f_{local} , implemented by a 3 layer, 1×1 convolutional block:

$$A_l = f_{\text{local}}(\Sigma_{G_l Y_l}, \Sigma_{G_l G_l}), b_l = \bar{Y}_l - A_l \odot \bar{G}_l \quad (12)$$

where covariances are determined as, $\Sigma_{G_l Y_l} = \overline{G_l Y_l} - \bar{G}_l \bar{Y}_l$, etc. Finally, we use our atrous residual block to implement the transformation function $F(X)$, and show that it confers substantial performance gains (Section 5.1). Overall, our guided filter consists of three trainable components, viz. F , f_μ and f_{local} .

3.3 Loss Function

L1 Loss. We employ Mean Absolute Error (or L1 loss) as our objective function. We empirically justify our choice L1 loss over other loss formulations (including MS-SSIM [72], perceptual [24] and adversarial [15] losses) in Section 5.2.

4 Experiments and Analysis

4.1 Dataset

Our network is trained on the POLED and TOLED datasets [75] provided by the UDC 2020 Image Restoration Challenge. Both datasets comprise of 300 images of size 1024×2048 , where 240 images are used for training, 30 for validation and 30 for testing in each track. We do not have access to any specific information of the forward model (such as the PSF or display profile), precluding usage of non-blind image restoration methods such as Wiener Filter [42].

4.2 Implementation Details

Model Architecture. LRNet comprises of 3 atrous residual groups, with 4 blocks each. The intermediate channel size in LRNet is set to 48. The training data is augmented with random horizontal flips, vertical flips and 180° rotations. All images are normalized to a range between -1 and 1. The AdamW [35] optimizer, with initial learning rate $\eta = 0.0003$, $\beta_1 = 0.9$ and $\beta_2 = 0.999$ is used. The learning rate is varied with epochs as per the cosine annealing scheduler with warm restarts [34]. We perform the first warm restart after 64 epochs, post which we double the duration of each annealing cycle. The models are trained using PyTorch [43] on 4 NVIDIA 1080Ti GPUs with a minibatch size of 4, for 960 epochs each.

Pre-training Strategy. To aid in faster convergence and boost performance, we pre-train our model with simulated data. The UDC dataset is created using monitor acquisition [75], where images from the DIV2K dataset [2] are displayed on a LCD monitor and captured by a camera mounted behind either glass

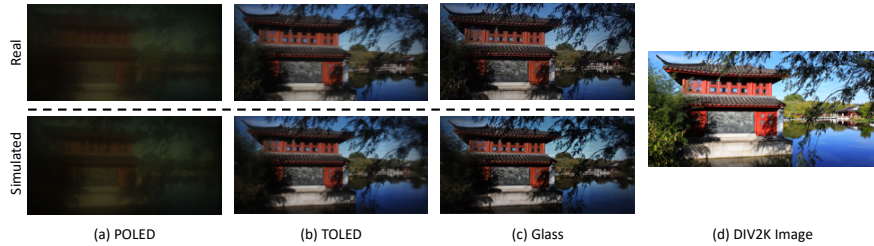


Fig. 5: **Pre-training using simulated data enhances performance.** We transform 800 DIV2K [2] images via a simulation network to various display measurements (Glass, TOLED and POLED). To train our simulation network, we use the misalignment tolerant CoBi [70] loss.

(considered ground-truth) or POLED/TOLED panels (low-quality images). To simulate data, we need to transform clean images from the DIV2K dataset to various display measurements (POLED, TOLED or glass).

Using Fresnel Propagation to simulate data with either the display profile or calibrated PSF can be inaccurate [75]. Instead, a shallow variant of our model is trained to transform 800 images from the DIV2K dataset to each measurement. Since DIV2K images do not align with display measurements, we leverage the Contextual Bilateral (CoBi) Loss [70], which can handle moderately misaligned image pairs. For two images P and Q , with $\{p_{ij}\}$ and $\{q_{ij}\}$ ($i \in [H], j \in [W]$) representing them as a grid of RGB intensities, CoBi loss can be written as:

$$\text{CoBi}(P, Q) = \frac{1}{HW} \sum_{i,j} \min_{k,l} [\mathbb{D}(p_{ij}, q_{kl}) + \gamma((i-k)^2 + (j-l)^2)] \quad (13)$$

where \mathbb{D} is any distance metric (we use cosine distance). γ allows CoBi to be flexible to image-pair misalignment. As seen in Figure 5, our simulated measurements closely match real measurements. Such an initialisation procedure gives our model (DAGF-PreTr) around 0.3 to 0.5 dB improvement in PSNR (Table 1). More simulation results can be found in the supplementary material.

4.3 Quantitative and Qualitative Analysis

Baseline Methods. Our method is compared against four image restoration methods: DGF [59], PANet [39], UNet [45] and FFA-Net [44]. DGF utilises a trainable guided filter for image transformation. For DGF, we use 9 layers in the CAN [11] backbone (instead of 5) for better performance. UNet is a popular architecture in image restoration. A variant of UNet with a double encoder [75] and 64 intermediate channels in the first block is used. PANet and FFA-Net are specifically designed architectures for image denoising and dehazing, respectively. Small patch sizes often provide little information for faithful restoration.

Table 1: **Quantitative comparison.** By directly training on megapixel images, our approach, DAGF significantly outperforms baselines. To further boost performance, we pre-train on simulated data (DAGF-PreTr). **Red** indicates the best and **Blue** the second best in the chosen metric (on validation set).

Method	#Params ↓	POLED			TOLED		
		PSNR ↑	SSIM ↑	LPIPS ↓	PSNR ↑	SSIM ↑	LPIPS ↓
PANet [39]	6.0M	26.22	0.908	0.308	35.712	0.972	0.147
FFA-Net [44]	1.6M	29.02	0.936	0.256	36.33	0.975	0.126
DGF [59]	0.4M	29.93	0.931	0.362	34.43	0.956	0.220
Unet [45]	8.9M	29.98	0.932	0.251	36.73	0.971	0.143
DAGF (Ours)	1.1M	33.29	0.952	0.236	37.27	0.973	0.141
DAGF-PreTr (Ours)	1.1M	33.79	0.958	0.225	37.57	0.973	0.140

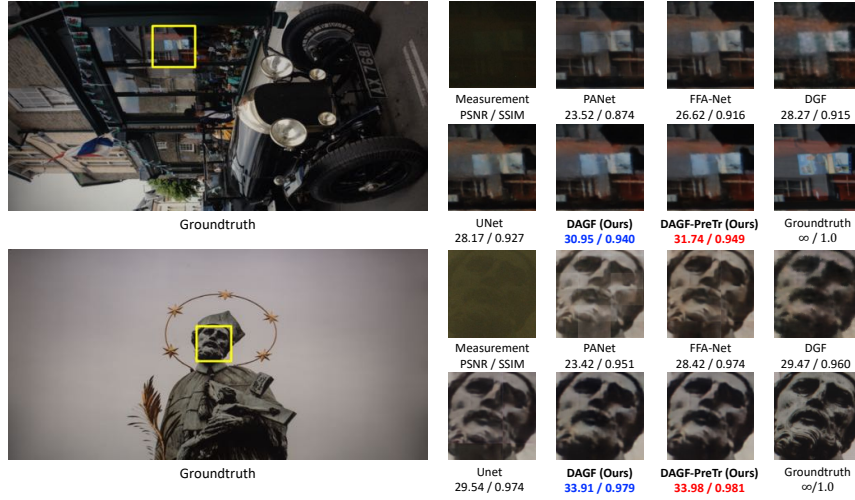
Hence, to make a fair comparison, a much larger patch size of 96×96 for PANet (compared to 48×48 in Mei *et al.* [39]), 256×512 for UNet (256×256 in Zhou *et al.* [75]) and 256×512 for FFA-Net (240×240 in Qin *et al.* [44]) is used.

Quantitative and Qualitative Discussion. All our methods are evaluated on PSNR, SSIM and the recently proposed LPIPS [69] metrics. Higher PSNR and SSIM score indicate better performance, while lower LPIPS indicates better perceptual quality. As seen in Table 1, our approach (DAGF) significantly outperforms the baselines, with an improvement of 3.2 dB and 0.5 dB over the closest baseline on POLED and TOLED measurements, respectively.

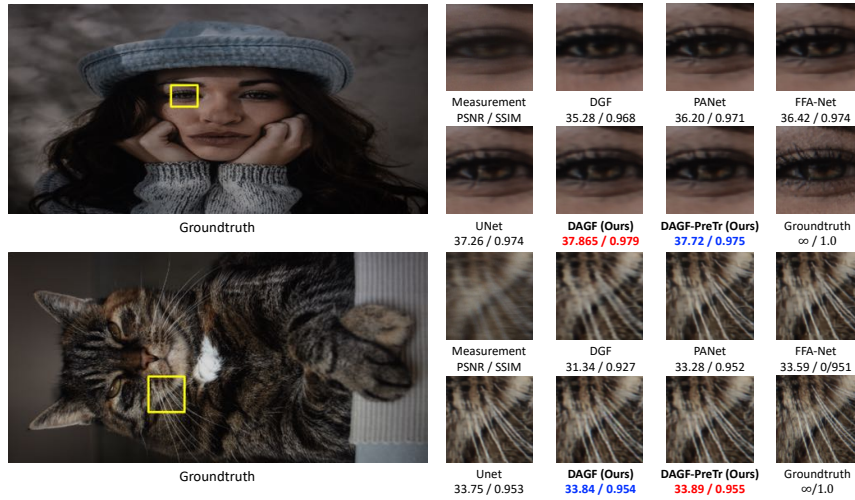
Our approach’s ability to directly train on megapixel images and hence aggregate contextual information over large receptive fields leads to a significant improvement. This is more evident on the POLED dataset, where patch based methods such as PANet, UNet and FFA-Net lack sufficient context despite using larger patch-sizes. With the exception of DGF, our approach also uses much lesser parameters. Visual comparisons in Figure 6 are consistent with our quantitative results. Our approach closely resembles groundtruth, having lesser artefacts and noise. Notably, in Figure 6a, we can observe line artefacts in patch based methods (further detailed in Section 5.1).

Challenge Results. This work is initially proposed for participating in the UDC 2020 Image Restoration Challenge [74]. For the challenge submission, geometric self-ensembling [47,51] is incorporated in DAGF-PreTr to boost performance, denoted in Table 2 as DAGF-PreTr+. Self-ensembling involves feeding various rotated and flipped versions of the input image to the network, and performing corresponding inverse transforms before averaging their outputs.

Quantitatively, our method ranks 2nd and 5th on the POLED and TOLED tracks, respectively (Table 2), proving that DAGF is effective at image restoration, especially in the severe degradation setting of POLED. While our approach is competitive on both tracks, there is scope to better adapt our model to moderate image degradation scenarios such as TOLED measurements.



(a) POLED dataset.



(b) TOLED dataset.

Fig. 6: **Qualitative results.** DAGF is considerably superior to patch based restoration methods [39,44,45], more evident on the severely degraded POLED measurements. Metrics evaluated on entire image. Zoom in to see details.

5 Further Analysis

To understand the role played by various components in DAGF, extensive ablation studies have been conducted. These experiments have been performed on downsized measurements, i.e., 512×1024 , in order to reduce training time.

Table 2: Comparison on UDC2020 Image Restoration Challenge. Red indicates the best performance and Blue the second best (on challenge test set).

POLED			TOLED		
Method	PSNR \uparrow	SSIM \uparrow	Method	PSNR \uparrow	SSIM \uparrow
First Method	32.99	0.957	First Method	38.23	0.980
DAGF-PreTr+ (Ours)	32.29	0.951	Second Method	38.18	0.980
Third Method	31.39	0.950	Third Method	38.13	0.980
Fourth Method	30.89	0.947	Fourth Method	37.83	0.978
Fifth Method	29.38	0.925	DAGF-PreTr+ (Ours)	36.91	0.973

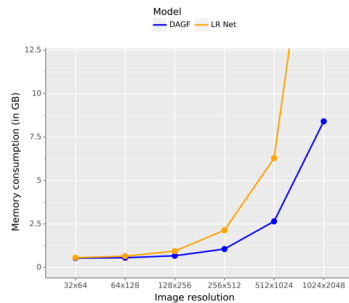


Fig. 7: Memory Consumption vs Image Size. Without a guided filter backbone, LRNet does not scale to larger image sizes.

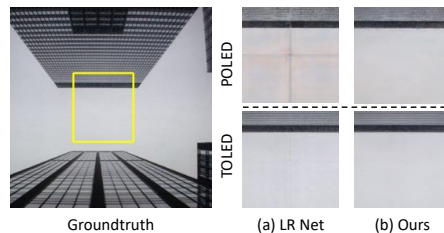


Fig. 8: Patch based methods lead to line artefacts, evident in the more challenging POLED output. In contrast, our method operates on the entire image and produces no such artefacts.

5.1 Effect of Guided Filter

The guided filter allows our approach to directly use high resolution images as input, as opposed to operating on patches or downsampled inputs. To demonstrated its utility, we compare the performance obtained with and without a guided filter. Without a guided filter framework, LRNet must be trained patch-wise, due to memory constraints (Figure 7). At test time, we assemble the output patch-wise.

Using a guided filter provides a significant benefit of 2.5 dB and 1.8 dB on POLED images and TOLED images, respectively (Table 3). Although marginally better LPIPS metrics indicate that LRNet produces more visually pleasing outputs, line artefacts can be observed in the outputs (Figure 8). Such artefacts are prominent in the more challenging POLED dataset. Alternative evaluation strategies for LRNet such as using overlapping patches followed by averaging, or feeding the entire high-resolution input results in blurry outputs and degrades performance.

Table 3 also features comparisons against other transformation functions $F(X)$. Experiments indicate a clear advantage in using our atrous residual block over either 1×1 or 3×3 conv layers proposed in Wu *et al.* [59].

Table 3: Using a **trainable guided filter** provides greater context by scaling to larger image dimensions.

Backbone	POLED			TOLED		
	PSNR \uparrow	SSIM \uparrow	LPIPS \downarrow	PSNR \uparrow	SSIM \uparrow	LPIPS \downarrow
No Guided Filter	30.14	0.938	0.212	33.92	0.963	0.132
Conv 1x1 Guided Filter	32.39	0.940	0.223	35.605	0.963	0.141
Conv 3x3 Guided Filter	32.50	0.942	0.220	35.84	0.965	0.150
Smoothed Atrous Block	32.87	0.946	0.216	35.87	0.966	0.147

5.2 Other Ablative Studies

All ablative results are presented in Table 4.

Smoothed Dilated Convolutions. Using either 3×3 convolutions or exponentially growing dilation rates [6,11] with the same number blocks leads to inferior performance. In contrast, parallel atrous convolutions lead to a larger receptive field at similar depth [5] and improves performance. We also verify that introducing a smoothing operation before atrous convolutions is beneficial, and qualitatively leads to fewer gridding (or checkerboard) artefacts [18,54,56].

Residual and Gated Connections. Consistent with Zhang *et al.* [71], removing local residual connections leads to a considerable degradation in performance. Similarly, gated attention, which can be perceived as a global residual connection with tunable weights, provides a noticeable performance gain.

Adaptive Normalisation. Using adaptive equivalents of batch-norm [22] or instance-norm [52] improves performance. Experiments indicate a marginal increase of adaptive batch-norm over adaptive instance-norm. However, since we use smaller minibatch sizes while training on 1024×2048 , we prefer adaptive instance-norm.

Channel attention. Unlike recent variants of channel attention [21,12,55,58], our implementation learns channel-wise weights, but does not capture inter-channel dependency. Experimenting with Efficient Channel Attention (ECA) [55] did not confer any substantial benefit, indicating that modelling inter-channel dependencies may not be important in our problem.

Loss functions. Compared to L1 loss, optimising MS-SSIM [72] loss can improve PSNR marginally, but tends to be unstable during the early stages of training. Perceptual [4] and adversarial [15] losses improve visual quality, reflected in better LPIPS scores, but degrade PSNR and SSIM metric performance [4]. Overall, L1 loss is a simple yet superior choice.

6 Conclusions

In this paper, we introduce a novel architecture for image restoration in Under Display Cameras. Deviating from existing patch-based image restoration methods, we show that there is a significant benefit in directly training on megapixel

Table 4: **Ablative Studies.** We experiment with various components present in our approach to justify our architecture choices.

Conditions				POLED			TOLED		
Smooth Atrous Convolutions									
Atrous	Parallel Atrous	Smooth Atrous		PSNR \uparrow	SSIM \uparrow	LPIPS \downarrow	PSNR \uparrow	SSIM \uparrow	LPIPS \downarrow
-	-	-		31.26	0.936	0.257	34.76	0.960	0.157
\checkmark	-	-		31.11	0.928	0.311	32.78	0.945	0.240
\checkmark	\checkmark	-		32.39	0.943	0.233	35.46	0.963	0.157
\checkmark	\checkmark	\checkmark		32.87	0.946	0.216	35.87	0.966	0.147
Residual and Gated Connections									
	Residual	Gated		PSNR \uparrow	SSIM \uparrow	LPIPS \downarrow	PSNR \uparrow	SSIM \uparrow	LPIPS \downarrow
	-	-		29.59	0.907	0.382	32.03	0.938	0.267
	\checkmark	-		32.19	0.941	0.255	35.14	0.961	0.162
	\checkmark	\checkmark		32.87	0.946	0.216	35.87	0.966	0.147
Normalization Layers									
BN [22]	IN [52]	ABN [11]	AIN	PSNR \uparrow	SSIM \uparrow	LPIPS \downarrow	PSNR \uparrow	SSIM \uparrow	LPIPS \downarrow
-	-	-	-	31.78	0.937	0.278	35.09	0.96	0.165
\checkmark	-	-	-	30.75	0.919	0.268	33.20	0.943	0.191
-	\checkmark	-	-	30.17	0.918	0.289	30.54	0.92	0.224
-	-	\checkmark	-	32.73	0.945	0.225	36.02	0.966	0.14
-	-	-	\checkmark	32.87	0.946	0.216	35.87	0.966	0.147
Channel Attention									
	ECA [55]	FFA [6]		PSNR \uparrow	SSIM \uparrow	LPIPS \downarrow	PSNR \uparrow	SSIM \uparrow	LPIPS \downarrow
	-	-		32.62	0.944	0.225	35.72	0.964	0.152
	\checkmark	-		32.66	0.944	0.232	35.98	0.966	0.143
	-	\checkmark		32.87	0.946	0.216	35.87	0.966	0.147
Loss Functions									
L1	MS-SSIM [72]	Percep. [24]	Adv. [15]	PSNR \uparrow	SSIM \uparrow	LPIPS \downarrow	PSNR \uparrow	SSIM \uparrow	LPIPS \downarrow
\checkmark	-	-	-	32.87	0.946	0.216	35.87	0.966	0.147
\checkmark	\checkmark	-	-	32.55	0.946	0.208	36.20	0.968	0.125
\checkmark	-	\checkmark	-	31.75	0.936	0.189	35.45	0.963	0.112
\checkmark	-	\checkmark	\checkmark	31.81	0.94	0.178	34.59	0.922	0.086

images. Incorporated in an end-to-end manner, a guided filter framework alleviates artefacts associated with patch based methods. We also show that a carefully designed low-resolution network utilising smoothed atrous convolutions and various attention blocks is essential for superior performance. Finally, we develop a simple simulation scheme to pre-train our model and boost performance. Our overall approach outperforms current models and attains 2nd place in the UDC 2020 Challenge- Track 2:POLED.

As evidenced by our superlative performance on POLED restoration, the proposed method is more suited for higher degree of image degradation. Future work could address modifications to better handle a variety of image degradation tasks. Another promising perspective is to make better use of simulated data, for instance, in a domain-adaptation framework.

Acknowledgements. The authors would like to thank Genesis Cloud for providing additional compute hours.

References

1. Abdelhamed, A., Affi, M., Timofte, R., Brown, M.S.: Ntire 2020 challenge on real image denoising: Dataset, methods and results. In: Proceedings of the IEEE/CVF Conference on Computer Vision and Pattern Recognition (CVPR) Workshops (June 2020)
2. Agustsson, E., Timofte, R.: Ntire 2017 challenge on single image super-resolution: Dataset and study. In: Proceedings of the IEEE Conference on Computer Vision and Pattern Recognition (CVPR) Workshops (July 2017)
3. Ancuti, C.O., Ancuti, C., Vasluianu, F.A., Timofte, R.: Ntire 2020 challenge on nonhomogeneous dehazing. In: Proceedings of the IEEE/CVF Conference on Computer Vision and Pattern Recognition (CVPR) Workshops (June 2020)
4. Blau, Y., Mechrez, R., Timofte, R., Michaeli, T., Zelnik-Manor, L.: The 2018 pirm challenge on perceptual image super-resolution. In: Proceedings of the European Conference on Computer Vision (ECCV) (September 2018)
5. Brehm, S., Scherer, S., Lienhart, R.: High-resolution dual-stage multi-level feature aggregation for single image and video deblurring. In: Proceedings of the IEEE/CVF Conference on Computer Vision and Pattern Recognition (CVPR) Workshops (June 2020)
6. Chen, D., He, M., Fan, Q., Liao, J., Zhang, L., Hou, D., Yuan, L., Hua, G.: Gated context aggregation network for image dehazing and deraining. In: Proceedings of the IEEE/CVF Winter Conference on Applications of Computer Vision (WACV) Workshops (March 2018)
7. Chen, J., Adams, A., Wadhwa, N., Hasinoff, S.W.: Bilateral guided upsampling. *ACM Transactions on Graphics (TOG)* **35**(6), 1–8 (2016)
8. Chen, L.C., Papandreou, G., Kokkinos, I., Murphy, K., Yuille, A.L.: Deeplab: Semantic image segmentation with deep convolutional nets, atrous convolution, and fully connected crfs. *IEEE Transactions on Pattern Analysis and Machine Intelligence* **40**(4), 834–848 (2017)
9. Chen, L.C., Papandreou, G., Schroff, F., Adam, H.: Rethinking atrous convolution for semantic image segmentation. *arXiv preprint arXiv:1706.05587* (2017)
10. Chen, L.C., Zhu, Y., Papandreou, G., Schroff, F., Adam, H.: Encoder-decoder with atrous separable convolution for semantic image segmentation. In: Proceedings of the European Conference on Computer Vision (ECCV) (September 2018)
11. Chen, Q., Xu, J., Koltun, V.: Fast image processing with fully-convolutional networks. In: Proceedings of the IEEE International Conference on Computer Vision (ICCV) (Oct 2017)
12. Chen, Y., Kalantidis, Y., Li, J., Yan, S., Feng, J.: A²-nets: Double attention networks. In: Advances in neural information processing systems (December 2018)
13. Gharbi, M., Chen, J., Barron, J.T., Hasinoff, S.W., Durand, F.: Deep bilateral learning for real-time image enhancement. *ACM Transactions on Graphics (TOG)* **36**(4), 118 (2017)
14. Gong, E., Pauly, J., Zaharchuk, G.: Boosting snr and/or resolution of arterial spin label (asl) imaging using multi-contrast approaches with multi-lateral guided filter and deep networks. In: Proceedings of the Annual Meeting of the International Society for Magnetic Resonance in Medicine, Honolulu, Hawaii (2017)
15. Goodfellow, I., Pouget-Abadie, J., Mirza, M., Xu, B., Warde-Farley, D., Ozair, S., Courville, A., Bengio, Y.: Generative adversarial nets. In: Advances in neural information processing systems (December 2014)

16. Gu, S., Li, Y., Gool, L.V., Timofte, R.: Self-guided network for fast image denoising. In: Proceedings of the IEEE/CVF International Conference on Computer Vision (ICCV) (October 2019)
17. Guo, Y., Han, S., Cao, H., Zhang, Y., Wang, Q.: Guided filter based deep recurrent neural networks for hyperspectral image classification. *Procedia Computer Science* **129**, 219–223 (2018)
18. Hamaguchi, R., Fujita, A., Nemoto, K., Imaizumi, T., Hikosaka, S.: Effective use of dilated convolutions for segmenting small object instances in remote sensing imagery. In: Proceedings of the IEEE/CVF Winter Conference on Applications of Computer Vision (WACV) Workshops (March 2018)
19. He, K., Sun, J., Tang, X.: Guided image filtering. *IEEE Transactions on Pattern Analysis and Machine Intelligence* **35**(6), 1397–1409 (2013)
20. He, K., Sun, J.: Fast guided filter. arXiv preprint arXiv:1505.00996 (2015)
21. Hu, J., Shen, L., Sun, G.: Squeeze-and-excitation networks. In: Proceedings of the IEEE Conference on Computer Vision and Pattern Recognition (CVPR) (June 2018)
22. Ioffe, S., Szegedy, C.: Batch normalization: Accelerating deep network training by reducing internal covariate shift. arXiv preprint arXiv:1502.03167 (2015)
23. Jiang, Y., Gong, X., Liu, D., Cheng, Y., Fang, C., Shen, X., Yang, J., Zhou, P., Wang, Z.: Enlightengan: Deep light enhancement without paired supervision. arXiv preprint arXiv:1906.06972 (2019)
24. Johnson, J., Alahi, A., Fei-Fei, L.: Perceptual losses for real-time style transfer and super-resolution. In: Proceedings of the European Conference on Computer Vision (ECCV) (October 2016)
25. Kim, D.W., Ryun Chung, J., Jung, S.W.: Grdn:grouped residual dense network for real image denoising and gan-based real-world noise modeling. In: Proceedings of the IEEE/CVF Conference on Computer Vision and Pattern Recognition (CVPR) Workshops (June 2019)
26. Kim, J., Lee, J.K., Lee, K.M.: Accurate image super-resolution using very deep convolutional networks. In: Proceedings of the IEEE Conference on Computer Vision and Pattern Recognition (CVPR) (June 2016)
27. Kopf, J., Cohen, M.F., Lischinski, D., Uyttendaele, M.: Joint bilateral upsampling. *ACM Transactions on Graphics (ToG)* **26**(3), 96–es (2007)
28. Kupyn, O., Martyniuk, T., Wu, J., Wang, Z.: Deblurgan-v2: Deblurring (orders-of-magnitude) faster and better. In: Proceedings of the IEEE/CVF International Conference on Computer Vision (ICCV) (October 2019)
29. Lehtinen, J., Munkberg, J., Hasselgren, J., Laine, S., Karras, T., Aittala, M., Aila, T.: Noise2noise: Learning image restoration without clean data. arXiv preprint arXiv:1803.04189 (2018)
30. Li, X., Wu, J., Lin, Z., Liu, H., Zha, H.: Recurrent squeeze-and-excitation context aggregation net for single image deraining. In: Proceedings of the European Conference on Computer Vision (ECCV) (September 2018)
31. Lim, B., Son, S., Kim, H., Nah, S., Mu Lee, K.: Enhanced deep residual networks for single image super-resolution. In: Proceedings of the IEEE Conference on Computer Vision and Pattern Recognition (CVPR) Workshops (July 2017)
32. Lin, D., Ji, Y., Lischinski, D., Cohen-Or, D., Huang, H.: Multi-scale context intertwining for semantic segmentation. In: Proceedings of the European Conference on Computer Vision (ECCV) (September 2018)
33. Lin, T.Y., Dollar, P., Girshick, R., He, K., Hariharan, B., Belongie, S.: Feature pyramid networks for object detection. In: Proceedings of the IEEE Conference on Computer Vision and Pattern Recognition (CVPR) (July 2017)

34. Loshchilov, I., Hutter, F.: Sgdr: Stochastic gradient descent with warm restarts. In: International Conference on Learning Representations (April 2017)
35. Loshchilov, I., Hutter, F.: Decoupled weight decay regularization. In: International Conference on Learning Representations (April 2019)
36. Lugmayr, A., Danelljan, M., Timofte, R.: Ntire 2020 challenge on real-world image super-resolution: Methods and results. In: Proceedings of the IEEE/CVF Conference on Computer Vision and Pattern Recognition (CVPR) Workshops (June 2020)
37. Mao, X., Shen, C., Yang, Y.B.: Image restoration using very deep convolutional encoder-decoder networks with symmetric skip connections. In: Advances in neural information processing systems (December 2016)
38. Marin, D., He, Z., Vajda, P., Chatterjee, P., Tsai, S., Yang, F., Boykov, Y.: Efficient segmentation: Learning downsampling near semantic boundaries. In: Proceedings of the IEEE/CVF International Conference on Computer Vision (ICCV) (October 2019)
39. Mei, Y., Fan, Y., Zhang, Y., Yu, J., Zhou, Y., Liu, D., Fu, Y., Huang, T.S., Shi, H.: Pyramid attention networks for image restoration. arXiv preprint arXiv:2004.13824 (2020)
40. Mostafa Kamal Sarker, M., Rashwan, H.A., Talavera, E., Furraka Banu, S., Radeva, P., Puig, D.: Macnet: Multi-scale atrous convolution networks for food places classification in egocentric photo-streams. In: Proceedings of the European Conference on Computer Vision (ECCV) Workshops (September 2018)
41. Nah, S., Son, S., Timofte, R., Lee, K.M.: Ntire 2020 challenge on image and video deblurring. In: Proceedings of the IEEE/CVF Conference on Computer Vision and Pattern Recognition (CVPR) Workshops (June 2020)
42. Orieux, F., Giovannelli, J.F., Rodet, T.: Bayesian estimation of regularization and point spread function parameters for wiener–hunt deconvolution. *JOSA A* **27**(7), 1593–1607 (2010)
43. Paszke, A., Gross, S., Massa, F., Lerer, A., Bradbury, J., Chanan, G., Killeen, T., Lin, Z., Gimelshein, N., Antiga, L., Desmaison, A., Kopf, A., Yang, E., DeVito, Z., Raison, M., Tejani, A., Chilamkurthy, S., Steiner, B., Fang, L., Bai, J., Chintala, S.: Pytorch: An imperative style, high-performance deep learning library. In: Advances in neural information processing systems (December 2019)
44. Qin, X., Wang, Z., Bai, Y., Xie, X., Jia, H.: Ffa-net: Feature fusion attention network for single image dehazing. In: AAAI (February 2020)
45. Ronneberger, O., Fischer, P., Brox, T.: U-net: Convolutional networks for biomedical image segmentation. In: Navab, N., Hornegger, J., Wells, W.M., Frangi, A.F. (eds.) *Medical Image Computing and Computer-Assisted Intervention – MICCAI 2015*. pp. 234–241. Springer International Publishing (2015)
46. Shi, W., Caballero, J., Huszar, F., Totz, J., Aitken, A.P., Bishop, R., Rueckert, D., Wang, Z.: Real-time single image and video super-resolution using an efficient sub-pixel convolutional neural network. In: Proceedings of the IEEE Conference on Computer Vision and Pattern Recognition (CVPR) (June 2016)
47. Sim, H., Kim, M.: A deep motion deblurring network based on per-pixel adaptive kernels with residual down-up and up-down modules. In: Proceedings of the IEEE/CVF Conference on Computer Vision and Pattern Recognition (CVPR) Workshops (June 2019)
48. Simonyan, K., Zisserman, A.: Very deep convolutional networks for large-scale image recognition. In: International Conference on Learning Representations (ICLR) (May 2015)

49. Tai, Y., Yang, J., Liu, X., Xu, C.: Memnet: A persistent memory network for image restoration. In: Proceedings of the IEEE International Conference on Computer Vision (ICCV) (Oct 2017)
50. Tao, X., Gao, H., Shen, X., Wang, J., Jia, J.: Scale-recurrent network for deep image deblurring. In: Proceedings of the IEEE Conference on Computer Vision and Pattern Recognition (CVPR) (June 2018)
51. Timofte, R., Rothe, R., Van Gool, L.: Seven ways to improve example-based single image super resolution. In: Proceedings of the IEEE Conference on Computer Vision and Pattern Recognition (CVPR) (June 2016)
52. Ulyanov, D., Vedaldi, A., Lempitsky, V.: Improved texture networks: Maximizing quality and diversity in feed-forward stylization and texture synthesis. In: Proceedings of the IEEE Conference on Computer Vision and Pattern Recognition (CVPR) (July 2017)
53. Ulyanov, D., Vedaldi, A., Lempitsky, V.: Deep image prior. In: Proceedings of the IEEE Conference on Computer Vision and Pattern Recognition (CVPR) (June 2018)
54. Wang, P., Chen, P., Yuan, Y., Liu, D., Huang, Z., Hou, X., Cottrell, G.: Understanding convolution for semantic segmentation. In: Proceedings of the IEEE/CVF Winter Conference on Applications of Computer Vision (WACV) Workshops (March 2018)
55. Wang, Q., Wu, B., Zhu, P., Li, P., Zuo, W., Hu, Q.: Eca-net: Efficient channel attention for deep convolutional neural networks. In: Proceedings of the IEEE/CVF Conference on Computer Vision and Pattern Recognition (CVPR) (June 2020)
56. Wang, Z., Ji, S.: Smoothed dilated convolutions for improved dense prediction. In: Proceedings of the 24th ACM SIGKDD International Conference on Knowledge Discovery & Data Mining. ACM (August 2018)
57. Wenke, I.G.: Organic light emitting diode (oled). Research gate (2016)
58. Woo, S., Park, J., Lee, J.Y., Kweon, I.S.: Cbam: Convolutional block attention module. In: Proceedings of the European Conference on Computer Vision (ECCV) (September 2018)
59. Wu, H., Zheng, S., Zhang, J., Huang, K.: Fast end-to-end trainable guided filter. In: Proceedings of the IEEE Conference on Computer Vision and Pattern Recognition (CVPR) (June 2018)
60. Xu, Y., Wu, L., Xie, Z., Chen, Z.: Building extraction in very high resolution remote sensing imagery using deep learning and guided filters. *Remote Sensing* **10**(1), 144 (2018)
61. Yu, F., Koltun, V.: Multi-scale context aggregation by dilated convolutions. In: International Conference on Learning Representations (ICLR) (May 2016)
62. Yu, F., Koltun, V., Funkhouser, T.: Dilated residual networks. In: Proceedings of the IEEE Conference on Computer Vision and Pattern Recognition (CVPR) (July 2017)
63. Zhang, H., Patel, V.M.: Densely connected pyramid dehazing network. In: Proceedings of the IEEE Conference on Computer Vision and Pattern Recognition (CVPR) (June 2018)
64. Zhang, H., Patel, V.M.: Density-aware single image de-raining using a multi-stream dense network. In: Proceedings of the IEEE Conference on Computer Vision and Pattern Recognition (CVPR) (June 2018)
65. Zhang, J., Pan, J., Lai, W.S., Lau, R.W.H., Yang, M.H.: Learning fully convolutional networks for iterative non-blind deconvolution. In: Proceedings of the IEEE Conference on Computer Vision and Pattern Recognition (CVPR) (July 2017)

66. Zhang, K., Zuo, W., Chen, Y., Meng, D., Zhang, L.: Beyond a gaussian denoiser: Residual learning of deep cnn for image denoising. *IEEE Transactions on Image Processing* **26**(7), 3142–3155 (2017)
67. Zhang, K., Zuo, W., Gu, S., Zhang, L.: Learning deep cnn denoiser prior for image restoration. In: *Proceedings of the IEEE Conference on Computer Vision and Pattern Recognition (CVPR)* (July 2017)
68. Zhang, K., Zuo, W., Zhang, L.: Ffdnet: Toward a fast and flexible solution for cnn-based image denoising. *IEEE Transactions on Image Processing* **27**(9), 4608–4622 (2018)
69. Zhang, R., Isola, P., Efros, A.A., Shechtman, E., Wang, O.: The unreasonable effectiveness of deep features as a perceptual metric. In: *Proceedings of the IEEE Conference on Computer Vision and Pattern Recognition (CVPR)* (June 2018)
70. Zhang, X., Chen, Q., Ng, R., Koltun, V.: Zoom to learn, learn to zoom. In: *Proceedings of the IEEE Conference on Computer Vision and Pattern Recognition (CVPR)* (June 2019)
71. Zhang, Y., Tian, Y., Kong, Y., Zhong, B., Fu, Y.: Residual dense network for image restoration. *IEEE Transactions on Pattern Analysis and Machine Intelligence* pp. 1–1 (2020)
72. Zhao, H., Gallo, O., Frosio, I., Kautz, J.: Loss functions for image restoration with neural networks. *IEEE Transactions on Computational Imaging* **3**(1), 47–57 (2016)
73. Zhao, H., Shi, J., Qi, X., Wang, X., Jia, J.: Pyramid scene parsing network. In: *Proceedings of the IEEE Conference on Computer Vision and Pattern Recognition (CVPR)* (July 2017)
74. Zhou, Y., Kwan, M., Tolentino, K., Emerton, N., Lim, S., Large, T., Fu, L., Pan, Z., Li, B., Yang, Q., Liu, Y., Tang, J., Ku, T., Ma, S., Hu, B., Wang, J., Puthussery, D., S, H.P., Kuriakose, M., V, J.C., Sundar, V., Hegde, S., Kothandaraman, D., Mitra, K., Jassal, A., Shah, N.A., Nathan, S., Rahel, N.A.E., Chen, D., Nie, S., Yin, S., Ma, C., Wang, H., Zhao, T., Zhao, S., Rego, J., Chen, H., Li, S., Hu, Z., Lau, K.W., Po, L.M., Yu, D., Rehman, Y.A.U., Li, Y., Xing, L.: Udc 2020 challenge on image restoration of under-display camera: Methods and results. *arXiv preprint arXiv:2008.07742* (2020)
75. Zhou, Y., Ren, D., Emerton, N., Lim, S., Large, T.: Image restoration for under-display camera. *arXiv preprint arXiv:2003.04857* (2020)

[Supplementary Material]

Deep Atrous Guided Filter for Image Restoration in Under Display Cameras

Varun Sundar*, Sumanth Hegde*, Divya Kothandaraman, and Kaushik Mitra

Indian Institute of Technology Madras

{varunsundar@smail, sumanth@smail, ee15b085@smail, kmitra@ee}.iitm.ac.in

<https://github.com/varun19299/deep-atrous-guided-filter>

1 Guided Filter Details

In this section, we present the algorithmic details of our trainable guided filter, which uses the high-resolution input as the guide image and the restored low-resolution output as the filtering input, to produce the high-resolution output via joint-upsampling.

Architecture details: We first detail the architectural choices made for the trainable components of the guided filter. Our implementation is similar to He *et al.* [2], except that the mean filter f_μ is implemented via a 3x3 convolutional layer and the transformation function $F(\cdot)$ via our atrous residual block. Finally, the local parameter estimator f_{local} consists of a 3 layer, 1×1 convolutional block, with adaptive normalisation layers and ReLU activations in between. Similar to Wu *et al.* [6], the guided filter is trained in an end-to-end manner with LRNet. The complete architecture of f_{local} is detailed in Table 1.

Table 1: **Architecture of f_{local} .**

Layer	Convolution	Adaptive Norm	ReLU	Input / Output Channel Size
1	1x1	✓	✓	3+3 / 32
2	1x1	✓	✓	32 / 32
3	1x1	-	-	32 / 3

Algorithm of the Guided Filter Network: The entire algorithm is outlined in Algorithm 1. Here, f_\uparrow denotes an upsampling operation (we use bilinear upsampling). $[\cdot, \cdot]$ denotes concatenation and \odot denotes the Hadamard product.

* Equal Contribution

Algorithm 1: Trainable Guided Filter Network

Notation: Learnt Mean Filter f_μ
Transformation Function F
Local Parameter Estimator f_{local}
Bilinear Upsampling f_\uparrow
Concatenation operation $[\cdot, \cdot]$

Input : Low-resolution Image X_l
High resolution Image X_h
Low-resolution Output Y_l

Output : High-resolution Output Y_h

- 1 $G_l = F(X_l)$, $G_h = F(X_h)$
- 2 $\overline{G_l} = f_\mu(G_l)$
 $\overline{Y_l} = f_\mu(Y_l)$
 $\overline{G_l^2} = f_\mu(G_l \odot G_l)$
 $\overline{G_l Y_l} = f_\mu(G_l \odot Y_l)$
- 3 $\Sigma_{G_l G_l} = \overline{G_l^2} - \overline{G_l} \odot \overline{G_l}$
 $\Sigma_{G_l Y_l} = \overline{G_l Y_l} - \overline{G_l} \odot \overline{Y_l}$
- 4 $A_l = f_{\text{local}}([\Sigma_{G_l G_l}, \Sigma_{G_l Y_l}])$
 $b_l = \overline{Y_l} - A_l \odot \overline{G_l}$
- 5 $A_h = f_\uparrow(A_l)$, $b_h = f_\uparrow(b_l)$
- 6 $Y_h = A_h \odot G_h + b_h$

2 Line Artefacts in Patch-Based Methods

Patch-based methods lead to line artefacts, especially evident in severe degradation scenarios. We attribute this to the limited context available to patch-based methods during training. Our approach plays a significant role in alleviating these artefacts. Expanding on the comparisons shown in Section 5.1 of the main paper, we show similar comparisons against the other patch-based baseline methods, viz. PANet [3], FFA-Net [4] and UNet [5] (Figure 1).

3 Simulation Dataset

We show more outputs from our simulation procedure in Figure 2, comparing it against corresponding real measurements. We can observe that our simulated outputs are perceptually similar to real measurements, and also bear similar artefacts such as low-light degradation in POLED and stripe bands in TOLED. Notice that while the simulated measurements align with the clean DIV2K [1] images, the real measurements do not.

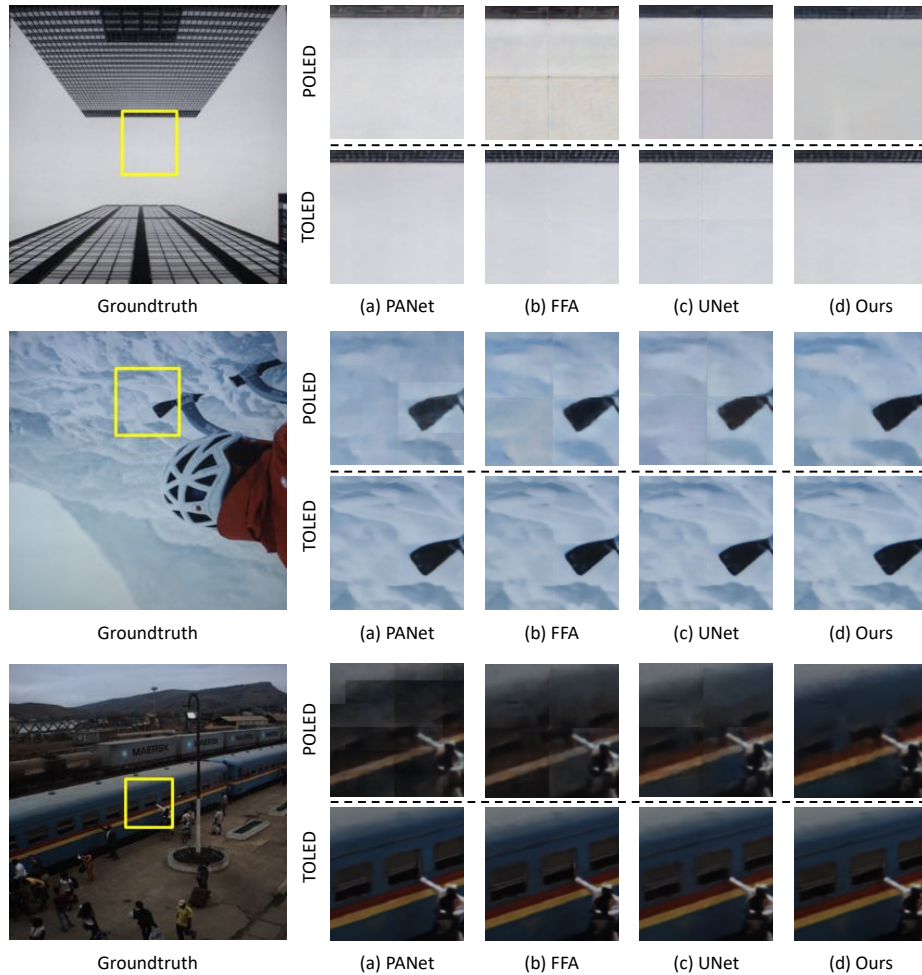


Fig. 1: **Line artefacts shown for patch-based baseline methods.** Our proposed method lacks such artefacts, since it directly trains on the entire megapixel input.

References

1. Agustsson, E., Timofte, R.: Ntire 2017 challenge on single image super-resolution: Dataset and study. In: Proceedings of the IEEE Conference on Computer Vision and Pattern Recognition (CVPR) Workshops (July 2017)
2. He, K., Sun, J.: Fast guided filter. arXiv preprint arXiv:1505.00996 (2015)
3. Mei, Y., Fan, Y., Zhang, Y., Yu, J., Zhou, Y., Liu, D., Fu, Y., Huang, T.S., Shi, H.: Pyramid attention networks for image restoration. arXiv preprint arXiv:2004.13824 (2020)

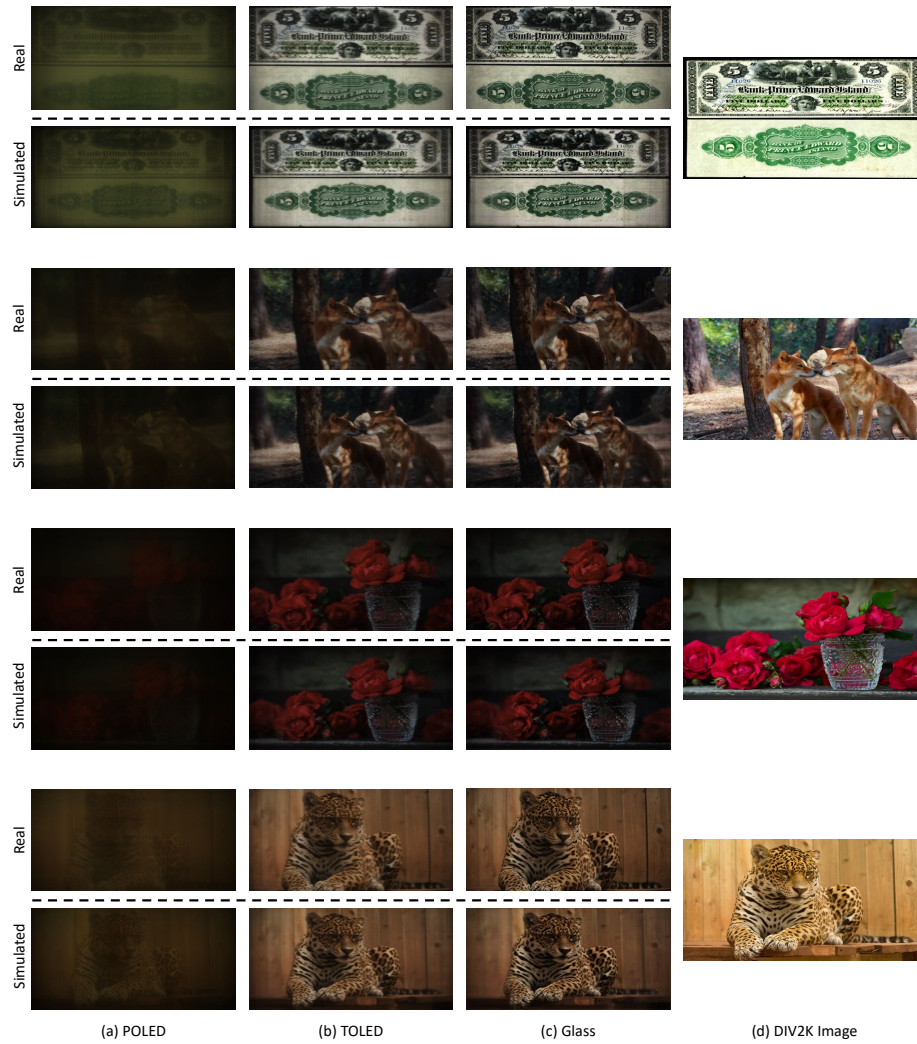


Fig. 2: More Simulation Outputs.

4. Qin, X., Wang, Z., Bai, Y., Xie, X., Jia, H.: Ffa-net: Feature fusion attention network for single image dehazing. In: AAAI (February 2020)
5. Ronneberger, O., Fischer, P., Brox, T.: U-net: Convolutional networks for biomedical image segmentation. In: Navab, N., Hornegger, J., Wells, W.M., Frangi, A.F. (eds.) Medical Image Computing and Computer-Assisted Intervention – MICCAI 2015. pp. 234–241. Springer International Publishing (2015)
6. Wu, H., Zheng, S., Zhang, J., Huang, K.: Fast end-to-end trainable guided filter. In: Proceedings of the IEEE Conference on Computer Vision and Pattern Recognition (CVPR) (June 2018)